Available online at www.sciencedirect.com
ScienceDirect
Journal of Power Sources 168 (2007) 218–228
JOURNAL OF POWER SOURCES
www.elsevier.com/locate/jpowsour

A two-phase non-isothermal mixed-domain PEM fuel cell model and its application to two-dimensional simulations

Hua Meng *

Center for Engineering and Scientific Computation, School of Aeronautics and Astronautics, P.O. Box 1455, Zhejiang University, Hangzhou, Zhejiang 310027, PR China

Received 18 January 2007; received in revised form 1 March 2007; accepted 1 March 2007
Available online 12 March 2007

Abstract

In this paper, a two-phase non-isothermal PEM fuel cell model based on the previously developed mixed-domain PEM fuel cell model with a consistent treatment of water transport in MEA has been established using the traditional two-fluid method. This two-phase multi-dimensional PEM fuel cell model could fully incorporate both the anode and cathode sides, properly account for the various water phases, including water vapor, water in the membrane phase, and liquid water, and truly enable numerical investigations of water and thermal management issues with the existence of condensation/evaporation interfaces in a PEM fuel cell. This two-phase model has been applied in this paper in a two-dimensional configuration to determine the appropriate condensation and evaporation rate coefficients and conduct extensive numerical studies concerning the effects of the inlet humidity condition and temperature variation on liquid water distribution with or without a condensation/evaporation interface.
© 2007 Elsevier B.V. All rights reserved.

Keywords: PEM fuel cell; Mixed-domain model; Two-phase transport; Water management; Thermal management

1. Introduction

Numerical modeling and simulation has been an important tool for facilitating PEM fuel cell design and optimization. Many multi-dimensional PEM fuel cell models have been developed in the past decade, and they can generally be categorized into two methods, namely the single-domain [1–9] and multi-domain [10–13] approaches. A mixed-domain model, which maintains a consistent treatment of water transport in the membrane-electrode assembly (MEA), has been recently developed [14] and further extended to investigate the effects of the fully coupled transport phenomena on fluid flows, species distributions, water transport processes, and detailed cell performances in PEM fuel cells [15].

Significant research efforts in the field of PEM fuel cell modeling and simulation have presently been focused on two-phase transport phenomena and the drastic effects on water management and cell performances. The two-phase PEM fuel cell models in the open literature account for the liquid water transport using either the multiphase mixture (M^2) model [12,16–20] or the traditional two-fluid model [9,21–24]. A common weakness in these models, however, remains in its inability to predict significant liquid saturation values in the porous gas diffusion layer (GDL) and catalyst layer (CL) and consequently the flooding effects in PEM fuel cells. In the work of Meng and Wang [25], a liquid droplet coverage model at the GDL and gas channel (GC) interface was proposed based on recent visualization experiments [26,27], and it was applied to successfully predict liquid water flooding dynamics.

Although progress has been made in multi-dimensional modeling of two-phase transport phenomena and flooding effects in PEM fuel cells, significant improvements are still needed, particularly in the areas of fully integrating two-phase flows with heat transfer phenomena and properly accounting for the effects of low-humidity inlet conditions on liquid water transport and flooding dynamics, and under both circumstances could exist the condensation/evaporation interfaces. These are remaining crucial research areas to be properly handled before the intricate interplays of water and thermal managements in PEM fuel cells could be fully investigated. Recently, Ju et al. [28] and Luo et al. [29] presented a three-dimensional two-phase isothermal PEM fuel cell model for investigating

* Tel.: +86 571 87953166; fax: +86 571 87953167.
E-mail address: menghua@zju.edu.cn.

0378-7753/$ – see front matter © 2007 Elsevier B.V. All rights reserved.
doi:10.1016/j.jpowsour.2007.03.012

Nomenclature

Nomenclature

a	water activity or stoichiometry coefficient
c	molar concentration (mol m^{-3})
C_p	constant-pressure heat capacity (J(kg K)$^{-1}$)
D	mass diffusivity (m^2 s^{-1})
D_λ	water content diffusivity (mol(m s)$^{-1}$)
EW	equivalent weight of the membrane (kg mol^{-1})
F	Faraday constant, 96,487C mol^{-1}
h_{pc}	condensation/evaporation parameter
h_{fg}	heat of vaporization (J kg^{-1})
i	current density vector (A m^{-2})
j	transfer current density (A m^{-3})
k	thermal conductivity (W(m K)$^{-1}$)
k_c	condensation rate coefficient (s^{-1})
k_e	evaporation rate coefficient (s^{-1} Pa^{-1})
K	permeability (m^2)
M	a symbol representing species
n_d	electro-osmotic drag coefficient
p	gas-phase pressure (Pa)
p_c	capillary pressure (Pa)
R_u	universal gas constant (J(mol K)$^{-1}$)
s	liquid saturation
S	source term
T	temperature (K)
u	gas-phase velocity (m s^{-1})
U_0	open-circuit potential (V)
V_{cell}	cell voltage (V)
W	molecular weight (kg mol^{-1})

Greek symbols

χ	mole fraction
ε	porosity
ε_m	fraction of the membrane phase in the catalyst layer
Φ	phase potential (V)
η	over-potential (V)
κ	proton conductivity (S m^{-1})
λ	water content
μ	viscosity (kg(m s)$^{-1}$)
θ_c	contact angle
ρ	gaseous density (kg m^{-3})
σ	electronic conductivity (S m^{-1}) or surface tension (N m^{-1})
τ	viscous stress tensor

Supercripts

cl	catalyst layer
eff	effective value
l	liquid phase
sat	saturation value
v	vapor phase

Subscripts

cl	catalyst layer
e	electrolyte or energy
g	gaseous phase
i	species
int	interfacial value
l	liquid
m	membrane
s	electron
sat	saturation value
w	water

the condensation/evaporation interfaces under low-humidity inlet conditions, and they successfully predicted the important feature of dry-wet-dry transition in PEM fuel cells. Non-isothermal two-phase calculations have also been provided in Ju [30]. All these simulations are based on the M^2 model.

In this paper, the pseudo single-phase mixed-domain PEM fuel cell model with a consistent treatment of water transport in MEA [14,15] is further extended to consider two-phase flows and liquid water transport based on the traditional two-fluid model. The important features of the present multi-dimensional two-phase mixed-domain PEM fuel cell model are mainly in the following areas: (1) consistent treatment of water transport in MEA with the presence of liquid water and thus appropriately including both the anode and cathode sides in the model, (2) proper account of the various water phases and their transport processes in a PEM fuel cell, including water vapor, liquid water, and water in the membrane phase or the dissolved water phase, (3) incorporating the liquid droplet coverage model at the GDL and gas channel interface [25] and thus capable of examining flooding dynamics and its effects on cell performances, and (4) fully coupling heat transfer phenomena with two-phase flows and consequently truly enabling numerical investigations of water and thermal management issues and their intricate interactions with the existence of a condensation/evaporation interface.

This two-phase model is applied in this paper in a two-dimensional configuration to determine the key parameters of condensation and evaporation rate coefficients and also to enable extensive parametric studies, focusing mainly on the effects of the inlet humidity condition and temperature variation on liquid water distribution with or without a condensation/evaporation interface.

2. Theoretical formulation

The complete conservation equations of this multi-dimensional two-phase mixed-domain PEM fuel cell model are presented in this section. First, the conservation equations of mass, momentum, and species concentrations in the gaseous phase are established.

Mass conservation:

$$\nabla \cdot (\rho \vec{u}) = 0 \tag{1}$$

Momentum conservation:

$$\frac{1}{\varepsilon^2(1-s)^2}\nabla \cdot (\rho \vec{u}\vec{u}) = -\nabla p + \nabla \cdot \tau + S_{\mathrm{u}} \tag{2}$$

Species conservation:

$$\nabla \cdot (\vec{u}c_i) = \nabla \cdot (D_i^{\mathrm{eff}} \nabla c_i) + S_i \tag{3}$$

In Eq. (2), the source term is added in the porous materials based on the Darcy's law considering the liquid water effect,

$$S_{\mathrm{u}} = -\frac{\mu}{K_{\mathrm{rg}}K}\vec{u} \tag{4}$$

The relative permeability is defined as [16]

$$K_{\mathrm{rg}} = (1-s)^3 \tag{5}$$

where the parameter, s, is the liquid saturation, defined as the ratio of the liquid volume to the pore volume [25].

In Eq. (3), based on the mixed-domain approach [14,15], the water vapor concentration is solved only in the gas channels, gas diffusion layers, and catalyst layers on both the anode and the cathode sides. Inside the membrane, a water content equation is solved, as presented later in this section. In the two catalyst layers, the dissolved water phase (water in the membrane phase) is assumed to be in thermodynamic phase equilibrium with water vapor, and its transport process is considered based on the "fictitious water concentration" treatment [14,31,32] using the following water diffusivity:

$$D_{\mathrm{w}}^{\mathrm{cl}} = \varepsilon_{\mathrm{cl}}^{1.5} D_{\mathrm{w}}^{\mathrm{cl,g}} + \varepsilon_{\mathrm{m}}^{1.5} D_{\lambda} \frac{R_{\mathrm{u}}T}{p_{\mathrm{sat}}} \frac{\mathrm{d}\lambda}{\mathrm{d}a} \tag{6}$$

Considering the liquid water effect, the effective gaseous species diffusion coefficients are further modified as

$$D_i^{\mathrm{eff}} = D_i(1-s)^{1.5} \tag{7}$$

The water vapor and the dissolved water phase in the catalyst layer and GDL could interact with liquid water through condensation/evaporation processes.

In the present two-phase model, water produced in the cathode catalyst layer is assumed to be in vapor phase as in [33] to be consistent with our previous pseudo single-phase method [14,15]. This is different from the assumption made in [21–24,34], but it should make no difference in the final results, i.e. the liquid saturation and temperature distributions, since the final states of water vapor and liquid water should approach their thermodynamic equilibrium conditions through condensation/evaporation processes in both methods, as discussed in detail later in this section and in Section 3. The source term in Eq. (3) can be expressed as

(a) for species except water

$$S_i = -\frac{a_i j}{nF} \tag{8a}$$

(b) for water vapor

$$S_{\mathrm{w}} = -\nabla \cdot \left(\frac{n_{\mathrm{d}}}{F}\vec{i}_{\mathrm{e}}\right) - \frac{a_{\mathrm{w}} j}{nF} - S_{\mathrm{vl}} \tag{8b}$$

In deriving Eq. (8) the electrochemical reactions are formulated in the following general form:

$$\sum_i a_i M_i = ne^- \tag{9}$$

In Eq. (8b), the variable, S_{vl}, is the volumetric condensation/evaporation rate, which is defined as

$$S_{\mathrm{vl}} = h_{\mathrm{pc}}(p^{\mathrm{v}} - p^{\mathrm{sat}}) \tag{10}$$

where the parameter, h_{pc}, is determined as [34]

$$h_{\mathrm{pc}} = \frac{k_{\mathrm{c}}\varepsilon(1-s)x_{\mathrm{v}}}{2R_{\mathrm{u}}T}\left[1 + \frac{|p^{\mathrm{v}} - p^{\mathrm{sat}}|}{p^{\mathrm{v}} - p^{\mathrm{sat}}}\right]$$

Table 1
Electrochemical and physical relationships

Description	Expression	Unit
Transfer current density	$j = aj_{0,\mathrm{a}}^{\mathrm{ref}}\left(\frac{c_{\mathrm{H_2}}}{c_{\mathrm{H_2,ref}}}\right)^{1/2}\left(\frac{\alpha_{\mathrm{a}}+\alpha_{\mathrm{c}}}{RT}\cdot F\cdot\eta\right)$ in anode side, $j = aj_{0,c}^{\mathrm{ref}}\left(\frac{c_{\mathrm{O_2}}}{c_{\mathrm{O_2,ref}}}\right)\exp\left(-\frac{\alpha_{\mathrm{c}}}{RT}\cdot F\cdot\eta\right)$ in cathode side	$\mathrm{A\,m^{-3}}$
Over potential	$\eta = \phi_{\mathrm{s}} - \phi_{\mathrm{e}}$ in anode side, $\eta = \phi_{\mathrm{s}} - \phi_{\mathrm{e}} - U_{\mathrm{o}}$ in cathode side	V
Open-circuit potential	$U_0 = 1.23 - 0.9\times10^{-3}(T-298)$	V
Electro-osmotic drag coefficient	$n_{\mathrm{d}} = \begin{cases} 1.0 \text{ for } \lambda \le 14 \\ 1.5/8(\lambda-14)+1.0, \text{ otherwise} \end{cases}$	
Water activity	$a = \frac{C_{\mathrm{w}}RT}{p^{\mathrm{sat}}}$	
Water saturation pressure	$\log_{10}p^{\mathrm{sat}} = -2.1794 + 0.02953(T-273.15) - 9.1837\times10^{-5}(T-273.15)^2 + 1.4454\times10^{-7}(T-273.15)^3$	atm
Membrane water diffusivity	$D_{\mathrm{w}}^{\mathrm{m}} = \begin{cases} 3.1\cdot10^{-7}\lambda(\mathrm{e}^{0.28\lambda}-1)\,\mathrm{e}^{[-2346/T]}, & 0<\lambda\le3 \\ 4.17\cdot10^{-8}\lambda(1+161\mathrm{e}^{-\lambda})\,\mathrm{e}^{[-2346/T]}, & \text{otherwise} \end{cases}$	$\mathrm{m^2\,s^{-1}}$
Water content diffusivity	$D_{\lambda} = \frac{\rho_{\mathrm{m}}}{\mathrm{EW}}D_{\mathrm{w}}^{\mathrm{m}}$	$\mathrm{mol\,m^{-1}\,s^{-1}}$
Proton conductivity	$\kappa = (0.5139\lambda - 0.326)\exp\left[1268\left(\frac{1}{303}-\frac{1}{T}\right)\right]$	$\mathrm{S\,m^{-1}}$

$$+\frac{k_e \varepsilon s \rho_l}{2W_l}\left[1-\frac{\left|p^v-p^{sat}\right|}{p^v-p^{sat}}\right] \tag{11}$$

The condensation and evaporation rate coefficients in Eq. (11), k_c and k_e, will be discussed and determined in the next section. The partial pressure of water vapor can be calculated as

$$p^v = C_w R_u T \tag{12}$$

An expression for calculating water saturation pressure is provided in Table 1.

All the other relevant physicochemical relations and properties can also be found in Table 1.

In the present two-phase model, the effects of liquid water on the gaseous species transport are taken into account using Eq. (7) in the porous GDL and catalyst layer. In fact, inside the catalyst layer, with the presence of the membrane phase, liquid water distribution and its effects on species transport and the electrochemical reactions involve complex physical processes, which are not clearly understood. In the open literature, there were attempts to consider liquid coverage on the membrane phase and the ensuing extra resistance exerting on species transport [34,35], i.e. the agglomerate approach, but they generally applied many simplifications and thus caused uncertainty in the model accuracy. In the present numerical studies, we neglect this phenomenon and focus mainly on the effects of the inlet humidity and temperature variation on liquid water distribution with condensation/evaporation interfaces in the porous materials. Furthermore, another reason for simplifying the catalyst layer model will be discussed in the next section when the numerical results are presented.

In this two-phase model, liquid water transport is taken into account using the traditional two-fluid method to add the flexibility for studying the finite-rate condensation/evaporation processes. As discussed in the next section, we will ensure the states of water vapor and liquid water closely approach their thermodynamic equilibrium conditions by choosing appropriate condensation and evaporation rate coefficients in this paper. It should be noted that the two-fluid method is mathematically equivalent to the multiphase mixture (M^2) model [36].

Next, the conservation equations of liquid water are presented.

Liquid mass conservation:

$$\nabla \cdot (\rho_l \vec{u}_l) = S_{vl} W_w \tag{13}$$

where an expression for the condensation/evaporation rate is presented in Eq. (10). In the porous materials, based on the Darcy's law, the liquid water velocity is derived as

$$\vec{u}_l = -\frac{K_{rl} K}{\mu^l}\nabla p^l \tag{14}$$

where the liquid pressure and the relative permeability are defined as [16]

$$p^l = p - p_c \tag{15}$$

and

$$K_{rl} = s^3 \tag{16}$$

Eqs. (13)–(15) can be combined to produce a conservation equation for the liquid saturation, which is

$$\nabla \cdot \left[\frac{\rho_l K_{rl} K}{\mu^l}\frac{\partial p_c}{\partial s}\nabla s\right] - \nabla \cdot \left[\frac{\rho_l K_{rl} K}{\mu^l}\nabla p\right] = S_{vl} W_w \tag{17}$$

The capillary pressure, p_c, can be further expressed as [16]

$$p_c = \left(\frac{\varepsilon}{K}\right)^{1/2} \sigma \cos\theta_c J(s) \tag{18}$$

where $J(s)$ is the well-known Leverett's function, which takes the following form for a hydrophobic porous material with a contact angle larger than 90° [37]:

$$J(s) = 1.417s - 2.120s^2 + 1.263s^3 \quad \theta_c > 90^\circ \tag{19}$$

Since numerical studies in this paper will be focused on two-phase transport phenomena in porous materials, liquid water transport in the gas channel and its interactions with the gaseous fluid-field are neglected. A mist flow model is used in Ref. [25].

Finally, the other conservation equations are derived as

Proton transport:

$$\nabla \cdot (\kappa^{eff} \nabla \phi_e) + S_e = 0 \tag{20}$$

Electron transport:

$$\nabla \cdot (\sigma^{eff} \nabla \phi_s) + S_s = 0 \tag{21}$$

Energy:

$$\nabla \cdot (\rho C_p \vec{u} T) + \nabla \cdot (\rho_l C_{p,l} \vec{u}_l T) = \nabla \cdot (k^{eff} \nabla T) + S_T \tag{22}$$

Water content conservation inside the membrane:

$$\nabla \cdot (D_\lambda \nabla \lambda) + S_\lambda = 0 \tag{23}$$

In Eqs. (20) and (21), the source terms can be expressed as

$$S_e = -S_s = j \tag{24}$$

In the energy equation, Eq. (22), the effects of species diffusion on temperature distribution has been neglected, and the source term is given as [38]

$$S_T = j\left(\eta + T\frac{dU_0}{dT}\right) + \frac{i^2}{\text{cond}} + h_{fg} W_w S_{vl} \tag{25}$$

where the second term inside the bracket is considered only on the cathode side. The parameter, cond, in Eq. (25) is either κ^{eff} or σ^{eff}, depending on the location in the fuel cell. The last term in Eq. (25) is the heat of vaporization.

In the water content equation inside the membrane, Eq. (23), the source term is

$$S_\lambda = -\nabla \cdot \left(\frac{n_d \vec{i}}{F}\right) \tag{26}$$

In addition, there are two boundary conditions at the interfaces between the membrane and the two catalyst layers, which are needed to connect the water content and the water vapor

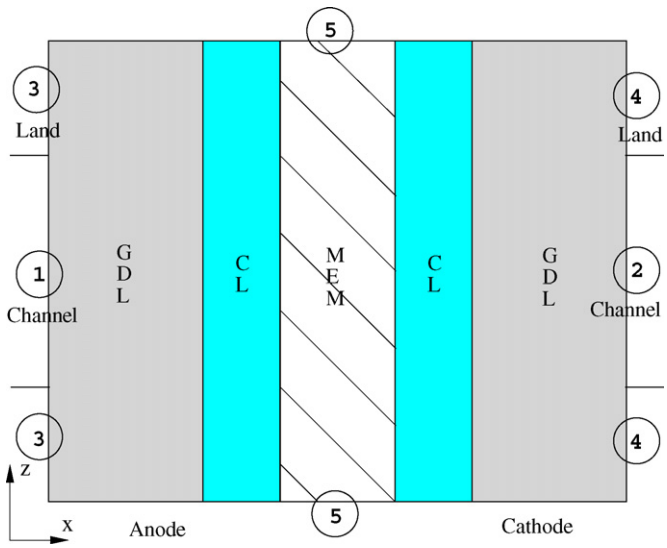

Fig. 1. A two-dimensional cross section and the related boundaries.

concentration equations [14,15]. The first boundary condition, assuming thermodynamic phase equilibrium at the interfaces, is [14,15]

when $s \leq 0$

$$\lambda = 0.043 + 17.81a - 39.85a^2 + 36.0a^3 \tag{27a}$$

when $s > 0$

$$\lambda = 14 + 2.8s \tag{27b}$$

where the parameter λ represents the water content on the membrane side of the interface while the parameters, a and s, the water activity and liquid saturation on the catalyst layer side of the interface, respectively. Eq. (27b) is proposed in Ref. [24].

The second boundary condition, ensuring water flux equality at the interfaces, is [14,15]

$$\left(-D_\lambda \nabla\lambda + \frac{n_d \vec{i}}{F}\right)\bigg|_m = \left(-D_w^{cl,eff}\nabla C_w + \frac{n_d \vec{i}}{F}\right)\bigg|_{cl} \tag{28}$$

where the effective water diffusivity in the two catalyst layers is provided in Eqs. (6) and (7).

The conservation equations, Eqs. (1)–(3), (17), and (20)–(23), constitute the present two-phase non-isothermal mixed-domain PEM fuel cell model. This model is applied for numerical simulations in a two-dimensional configuration, as shown in Fig. 1, to determine the condensation/evaporation rate coefficients, and also to make extensive parametric studies. The computational domain includes five regions, namely the gas diffusion layers and catalyst layers on both the anode and cathode sides, and the membrane. In the present two-dimensional simulation, since fluid flows in gas channels are neglected, the gaseous velocity and pressure are not computed. This simplification is valid based on the theoretical and numerical analyses of the Peclet number in the porous materials in [15,39].

There are five boundary conditions to be specified, as shown in Fig. 1. Boundary 1 is at the GDL and gas channel interface on the anode side. The boundary conditions are defined as

$$C_i = C_{i,0} \tag{29a}$$

$$s = s_{int} \tag{29b}$$

$$\frac{\partial \phi_e}{\partial x} = \frac{\partial \phi_s}{\partial x} = 0 \tag{29c}$$

$$\frac{\partial T}{\partial x} = 0 \tag{29d}$$

where the parameters, $C_{i,0}$ and s_{int}, are specified values. In Eq. (29d), the heat flux is set as zero since the prior numerical calculations indicate that the heat transfer rate through this interface is very small [38].

Boundary 2 is at the GDL and gas channel interface on the cathode side, the same type of boundary conditions as those in Eq. (29) are specified, and they are not repeated here.

Boundary 3 is at the interface between the GDL and the current-collecting land on the anode side. The boundary conditions are defined as

$$\frac{\partial C_i}{\partial x} = 0 \tag{30a}$$

$$\frac{\partial s}{\partial x} = 0 \tag{30b}$$

$$\frac{\partial \phi_e}{\partial x} = 0 \tag{30c}$$

$$\phi_s = 0 \tag{30d}$$

$$T = T_0 \tag{30e}$$

Boundary 4 is at the interface between the GDL and the current-collecting land on the cathode side. The same type of boundary conditions as those in Eq. (30) can be specified except for the one with the electronic phase potential, which becomes

$$\phi_s = V_{cell} \tag{31}$$

At boundary 5, the symmetric boundary conditions are used for all the variables.

3. Result and discussion

The present two-phase non-isothermal mixed-domain PEM fuel cell model has been implemented into a commercial CFD package, Fluent, through its user coding capabilities and applied herein for two-dimensional numerical simulations, as shown in Fig. 1. The geometric parameters of the fuel cell are listed in Table 2.

The fuel cell is operated at 2 atm on both the anode and cathode sides. Hydrogen and water vapor is fed into the anode while air and water vapor into the cathode. For all the calculations carried out in this paper, the cell voltage, V_{cell}, is fixed at 0.65 V, and the boundary temperature at 80 °C. In order to investigate the effect of the inlet humidity conditions on liquid water distributions, three cases have been designed, as listed in Table 3. Based on these operation conditions, the inlet species concentrations can be easily determined and specified at boundaries 1

Table 2
Cell geometric parameters

Fuel cell geometry [mm]	
Layer thickness	
Diffusion	0.3
Catalyst	0.01
Membrane	0.025
Land width	0.5
Channel width	1.0
Computational cell numbers	∼1600

and 2. Therefore, the present two-dimensional numerical calculations simulate a cross section perpendicular to the membrane at the inlet of a PEM fuel cell. The other relevant physical and transport parameters are provided in Table 4. Careful grid independence study has been conducted before extensive numerical investigations, and a total of 1600 computational cells have been used in the present calculations.

Numerical studies are first conducted to determine an appropriate condensation rate coefficient, k_c, which is related to the surface to volume ratio in a porous material [33]. The calculations are based on fully humidified inlet conditions, case 1 in Table 3, with a constant cell temperature of 80 °C. This case is chosen because no evaporation process occurs and thus the evaporation rate coefficient is irrelevant. Fig. 2 illustrates the liquid saturation distributions in cathode GDL and catalyst layer under three different condensation rate coefficients with a zero liquid saturation value specified at the boundaries 1 and 2. When the condensation rate coefficient increases from 500 to 2000 s^{-1}, the maximum liquid saturation increases more than 20%, indicating the results are dependent on this parameter. Increasing the condensation rate from 2000 to 5000 s^{-1} only brings around 6% increase of the maximum liquid saturation. Further increasing the condensation rate coefficient could hardly cause any increase of the maximum liquid saturation and variation of the liquid water distribution. The same conclusion could be drawn from Fig. 3, in which the water vapor concentrations under three corresponding conditions are presented. Fig. 3c shows clearly that the water vapor concentration approaches its thermodynamic equilibrium value at 15.9 mol m^{-3}, with only slight over-saturation. These results conclude that numerical results are independent of the condensation rate coefficient once it reaches a value of 5000 s^{-1}. Based on the present parametric studies and the detailed theoretical analyses in Ref. [33], a condensation rate coefficient at 5000 s^{-1} is considered as an appropriate parameter and is thus chosen in the present two-phase PEM fuel cell modeling. Using this condensation rate coefficient, the calculated water vapor concentration and liquid water saturation approach the thermodynamic equilibrium condition.

Table 4
Physicochemical parameters

Anode volumetric exchange current density, aj_0 (A m^{-3})	1.0E+9
Cathode volumetric exchange current density, aj_0 (A m^{-3})	1.0E+4
Reference hydrogen concentration, C_{H_2} (mol m^{-3})	40
Reference oxygen concentration, C_{O_2} (mol m^{-3})	40
Anode transfer coefficients	$\alpha_a = \alpha_c = 1$
Cathode transfer coefficient	$\alpha_c = 1$
Faraday constant, F (C mol^{-1})	96487
GDL porosity	0.6
Porosity of catalyst layer	0.12
Volume fraction of ionomer in catalyst layer	0.4
GDL permeability (m^2)	1.0E−12
Catalyst layer permeability (m^2)	1.0E−13
Equivalent weight of ionomer (kg mol^{-1})	1.1
Dry membrane density (kg m^{-3})	1980
Electronic conductivity in current collector (S m^{-1})	20,000
Effective electronic conductivity in GDL (S m^{-1})	5000
Operation pressure (atm)	2
Condensation rate coefficient (s^{-1})	5000
Evaporation rate coefficient (s^{-1} Pa^{-1})	1.0E−4
Liquid water density (kg m^{-3})	1000
Liquid water viscosity (Ns m^{-2})	3.5E−4
Surface tension (N m^{-1})	6.25E−2
Contact angle in GDL	110
Contact angle in CL	95
Thermal conductivity of current collector (W m^{-1} K^{-1})	20
Thermal conductivity of the membrane (W m^{-1} K^{-1})	0.5
Heat of vaporization (J kg^{-1})	2.3E+6

Next, parametric studies are conducted to determine an appropriate evaporation rate coefficient, k_e. The calculations are based on case 3 in Table 3 under an isothermal condition at 80 °C. Liquid saturation distributions with condensation/evaporation interfaces under three different evaporation rate coefficients are illustrated in Fig. 4. Decreasing the evaporation rate coefficient by an order of magnitude, from 1×10^{-3} to 1×10^{-4} (Pa s)$^{-1}$, brings no difference in the maximum liquid saturation value and the liquid water distribution around that region. However, decreasing the evaporation rate coefficient would result in a slightly larger liquid water distribution region. In the present two-phase model, an evaporation rate coefficient of 1×10^{-4} (Pa s)$^{-1}$ is chosen as it makes the condensation and evaporation parts of the phase-change parameter in Eq. (11), h_{pc}, at the same order of magnitude.

After the condensation/evaporation rate coefficients are determined, the two-phase model is then applied to study the effect of the liquid droplet coverage at the GDL and gas channel

Table 3
Inlet humidification temperature and relative humidity at 80 °C (the fully humidified water vapor concentration is 15.9 mol m^{-3})

Case number	Anode		Cathode	
	Humidification temperature (°C)	Relative humidity (%)	Humidification temperature (°C)	Relative humidity (%)
Case 1	80	100	80	100
Case 2	80	100	75	81
Case 3	80	100	70	66

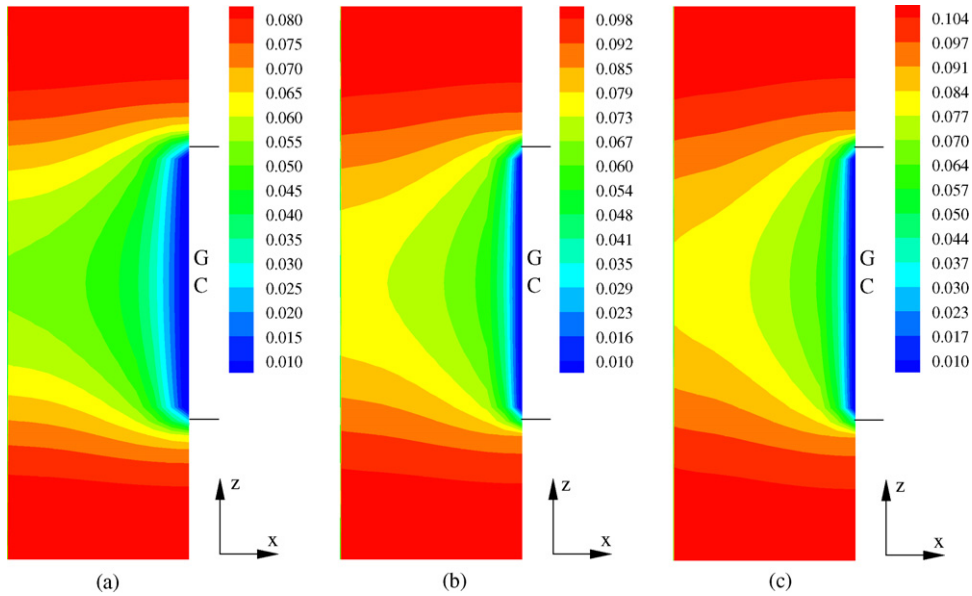

Fig. 2. Liquid saturation distributions at different condensation rate coefficients: (a) 500 s^{-1}, (b) 2000 s^{-1}, and (c) 5000 s^{-1}.

(GC) interface on liquid water distribution and cell performance through specifying different liquid saturation values at boundary 2, a phenomenon also discussed in Ref. [25]. In Fig. 5, increasing the liquid saturation value at the GDL/GC interface on the cathode side, meaning more liquid droplet attached at the GDL/GC interface [25], the maximum liquid saturation in the GDL and catalyst layer on the cathode side increases drastically while the liquid saturation gradient decreases, a phenomena resulting from a much stronger capillary-driven flow in the porous materials at a higher liquid saturation value. Similar results are also presented in Refs. [25,34]. The effect of the liquid droplet coverage at the GDL/GC interface on cell performance is depicted in Fig. 6, in which current density distributions along the lateral direction at three different liquid saturation boundary values are presented. Increased liquid saturation values in the porous materials with increased liquid saturation boundary values on the cathode side reduce the cell performance. For example, increasing the parameter, s_{int}, from 0 to 0.35, decreases the cell performance by more than 10%. Furthermore, current density decreases more significantly under the land than under the gas channel, a result attributable to extra resistance for oxygen transport in the region. It should be emphasized that since this is a two-dimensional calculation without the contact resistance for the electronic transport, the cell performance obtained is thus higher than the practical value, but this will not affect the present numerical investigations.

The effect of the inlet humidity conditions on the cathode side on liquid water distributions is clearly illustrated in Fig. 7, in

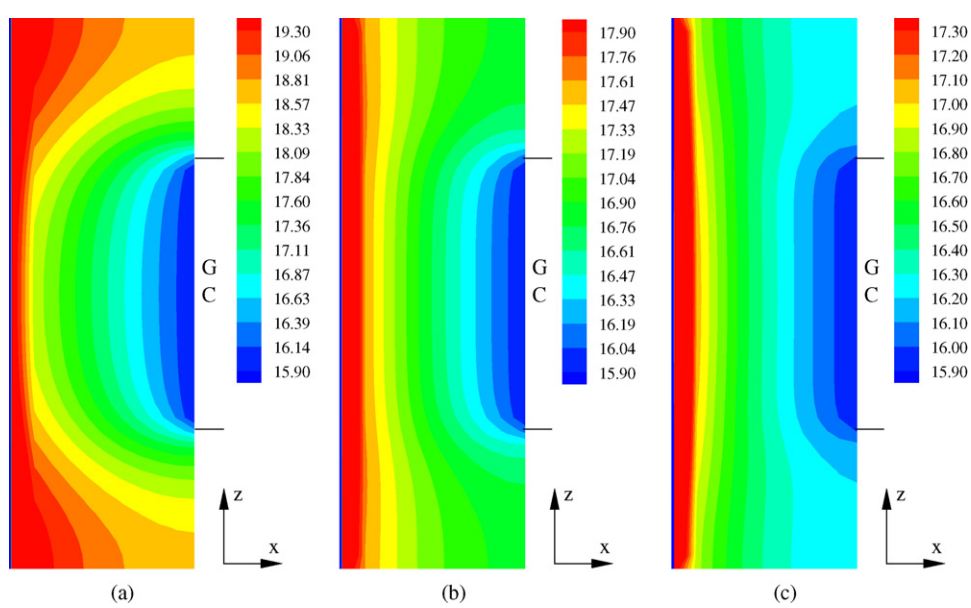

Fig. 3. Distributions of water vapor concentration at different condensation rate coefficients: (a) 500 s^{-1}, (b) 2000 s^{-1}, and (c) 5000 s^{-1}.

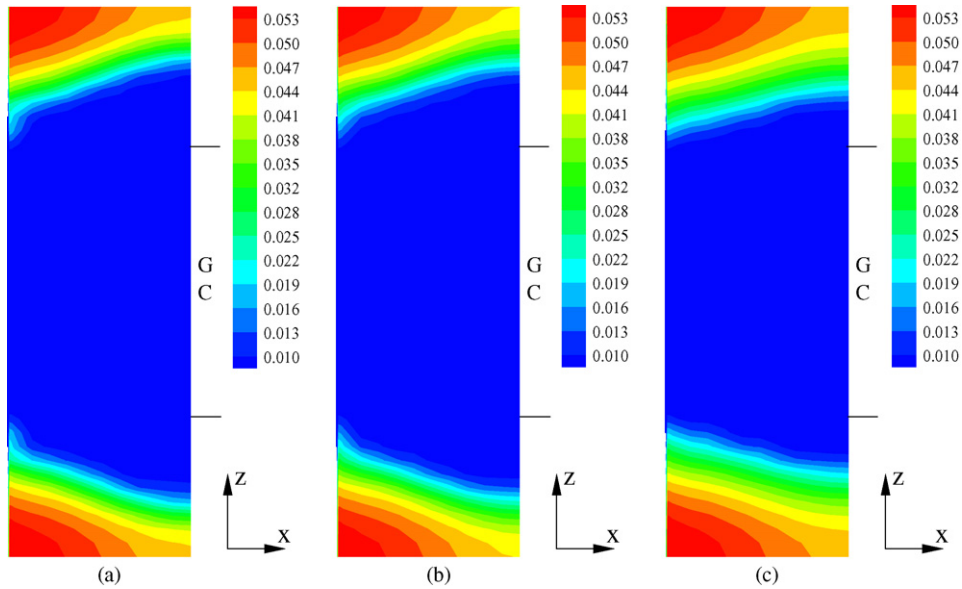

Fig. 4. Liquid saturation distributions at different evaporation rate coefficients: (a) 1.0E−3 s^{-1} Pa^{-1}, (b) 5.0E−4 s^{-1} Pa^{-1}, and (c) 1.0E−4 s^{-1} Pa^{-1}.

which results correspond to the three cases in Table 3 with a constant cell temperature of 80 °C are shown. With a low humidity inlet condition at a humidification temperature of 70 °C, liquid water only exists under the two land areas while the large area under the gas channel is at dry condition. The condensation/evaporation interface is well captured and can be clearly seen in Fig. 7a. Increasing the inlet humidification temperature on the cathode side to 75 °C results in drastic decrease of the dry region, and now the condensation/evaporation interface is completely under the gas channel, as shown in Fig. 7b. The dry region disappears under the fully humidified inlet condition as expected in Fig. 7c. Three-dimensional simulations predicting dry-wet-dry transitions in PEM fuel cells have recently been studied in Refs. [28,29].

Fully integrating water transport, including possibly liquid water transport, with heat transfer phenomena is crucial for simultaneously investigating water and thermal management issues in a PEM fuel cell. As discussed in Ref. [40], since there are uncertainties concerning the GDL thermal conductivity, parametric studies using two different thermal conductivities at 3 and 1.5 $W(m\,K)^{-1}$ are carried out in the present numerical simulations. The calculations correspond to case 1 in Table 3 with the boundary temperature defined at 80 °C. The temperature distributions produced using the two different thermal conductivities are displayed in Fig. 8. As expected, decreasing the GDL thermal conductivity increases temperature in the porous materials on both the anode and cathode sides. With a thermal conductivity at 1.5 $W(m\,K)^{-1}$, the maximum tempera-

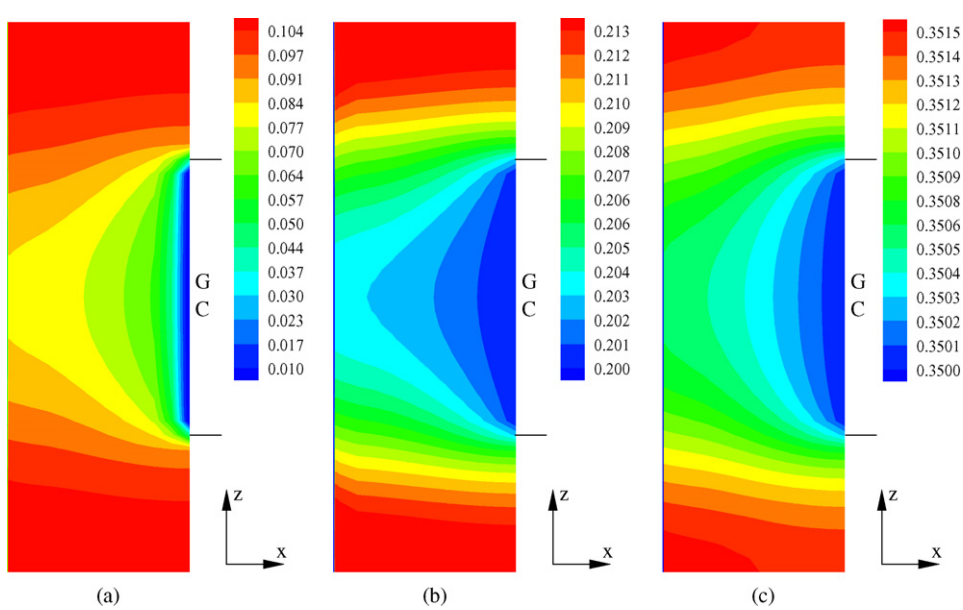

Fig. 5. Liquid saturation distributions with different liquid saturation values defined at the GDL/GC interface on the cathode side: (a) 0, (b) 0.2, and (c) 0.35.

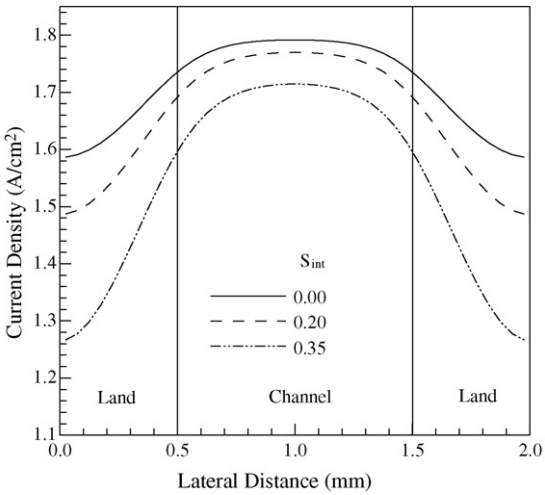

Fig. 6. Effect of liquid saturation value at the GDL/GC interface on the cathode side on current distribution in the lateral direction.

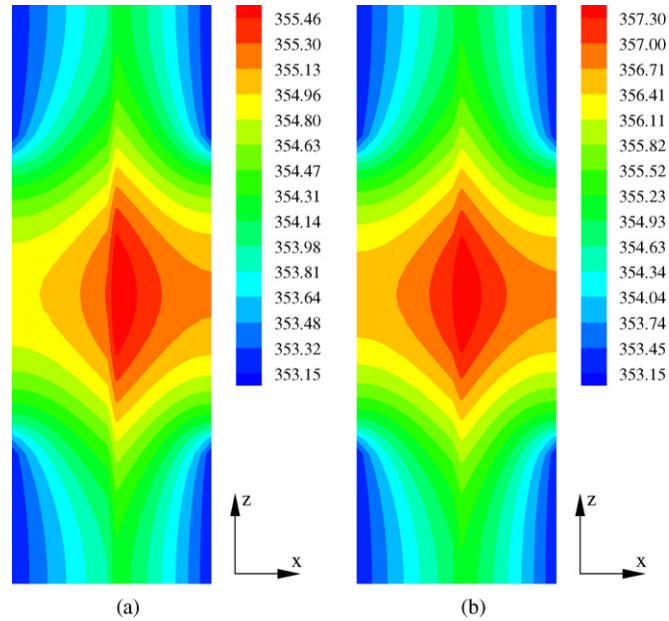

Fig. 8. Temperature distributions under two different thermal conductivities of the porous materials: (a) 3 W(m K)$^{-1}$ and (b) 1.5 W(m K)$^{-1}$.

ture rise is more than 4 °C under the gas channel, as shown in Fig. 8b. It should be emphasized that, in this case, the condensation and evaporation of liquid water does not contribute to the overall energy release but only serve to adjust the temperature distributions since condensation and evaporation energy completely cancel each other, as clearly indicated in Figs. 9c and 10b.

The non-isothermal effect on liquid water distribution is displayed in Fig. 9, in which the liquid saturation distributions corresponding to two different thermal conductivities are compared with that under the isothermal condition. With a thermal conductivity of 3 W(m K)$^{-1}$, the temperature increase is not sufficient to cause a dry region in GDL and catalyst layer on the cathode side although it does bring down the maximum liquid saturation, change liquid water distribution, and cause liquid water evaporation in a region near the GDL and gas channel interface, as shown in Fig. 10a. The evaporation process occurs owing to the increased liquid saturation pressure with the increased temperature. As indicated in Eqs. (10) and (11), the evaporation rate is driven by the difference between the partial pressure of water vapor and its saturation value, and also controlled by the liquid saturation variation.

As illustrated in Fig. 9c, with a thermal conductivity at 1.5 W(m K)$^{-1}$, the temperature rise in the porous materials produces a dry region directly under the gas channel, while the water vapor concentration at boundary 2 remains at 15.9 mol m^{-3}, a fully humidified value at 80 °C. As discussed in Ref. [40], a thermal conductivity of 1.5 W(m K)$^{-1}$ is a typical value in carbon

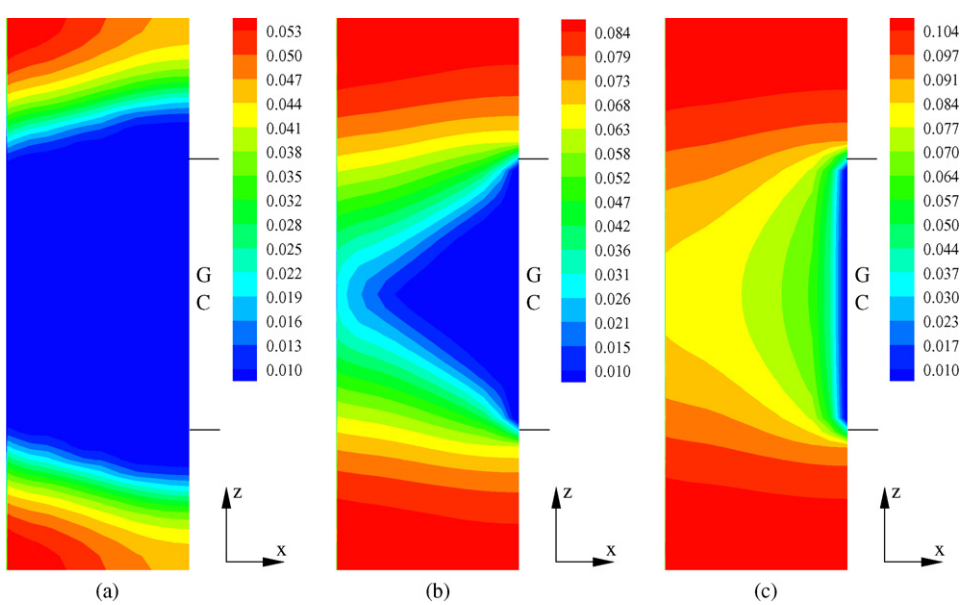

Fig. 7. Effect of inlet humidification temperature on liquid saturation distribution at a constant cell temperature of 80 °C: (a) 70 °C, (b) 75 °C, and (c) 80 °C.

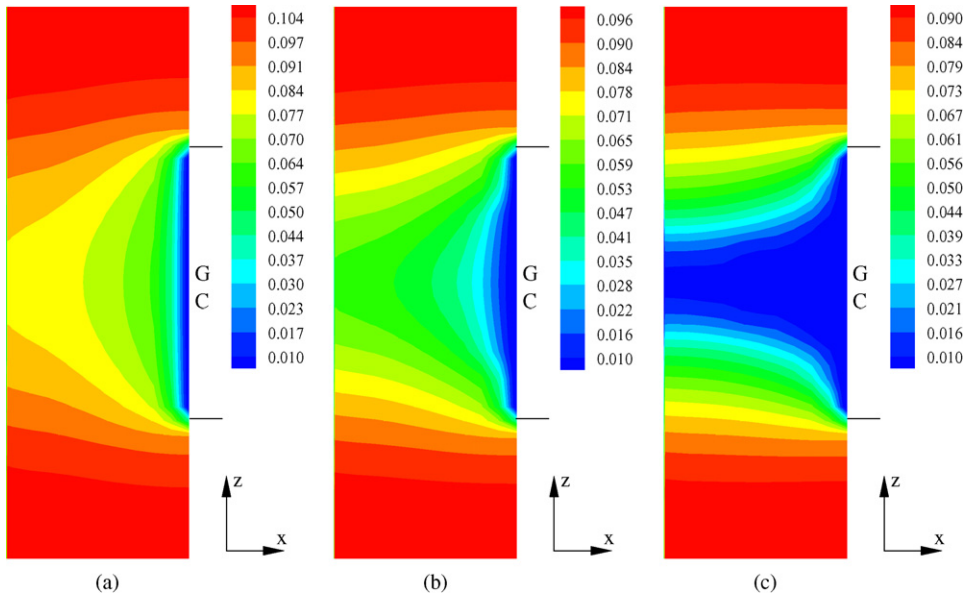

Fig. 9. Effect of thermal conductivity of the porous material on liquid saturation distribution: (a) isothermal case, (b) 3 W(m K)$^{-1}$, and (c) 1.5 W(m K)$^{-1}$.

paper. If the thermal contact resistance is further considered, the liquid water distribution in Fig. 9c should represent the normal situations in a PEM fuel cell at the inlet region. In fact, in both the experimental results in Refs. [27,41], there was hardly any liquid water observed under the gas channel in the inlet region, and in Ref. [27], liquid droplet emergence from the GDL was only observable near the exit region. Further downstream along the cathode gas channel, with the decrease of the current density and consequently decreased temperature and with the water vapor in the gas channel becoming over-saturated, the dry region under the gas channel would disappear, consistent with the experimental observations. This interesting phenomenon will be further investigated in the future three-dimensional numerical simulations.

Fig. 10 shows the distributions of the condensation and evaporation source terms, with a positive value for condensation and a negative one for evaporation. In both figures, in addition to the heat pipe phenomenon discussed in Ref. [20], that is evaporation process in the catalyst layer region (in our case the evaporation process is assumed to occur instantly since water is produced in the gaseous phase) carries out heat which is released when water vapor condenses near the current-collecting land, another heat pipe phenomenon also exists, that is evaporation process in the region near the gas channel carries out heat which is then released when water vapor condenses near the current-collecting land.

Furthermore, in Fig. 10 and particularly in Fig. 10b, liquid water is found to be produced inside the GDL away from the catalyst layer. Since temperature is sufficiently high in the catalyst layer, even if water produced by the electrochemical reaction is assumed to be in the liquid phase, it should be evaporated and as a result, only very small amount of liquid water could exist inside the catalyst layer at the inlet region. This is a result in favor of simplifying the liquid water modeling efforts in catalyst layer, as is the case in the present two-phase model.

Liquid water is produced in the GDL mainly in two regions; one is near the land owing to the low temperature in this region and another further inside the GDL but still away from the catalyst layer, as shown in Fig. 10. In the open literature, the role of the micro-porous layer (MPL) for improving liquid flooding and cell performance has been discussed by a number of researchers based on numerical analyses of the liquid water transport processes [33,42]. Based on the present numerical results in Fig. 10, we hypothesize that at least at the inlet region of the cell, a role of the MPL is to prevent liquid water from entering the catalyst layer and therefore prevent severe liquid flooding in the region, since liquid water transport preferentially selects larger pores in

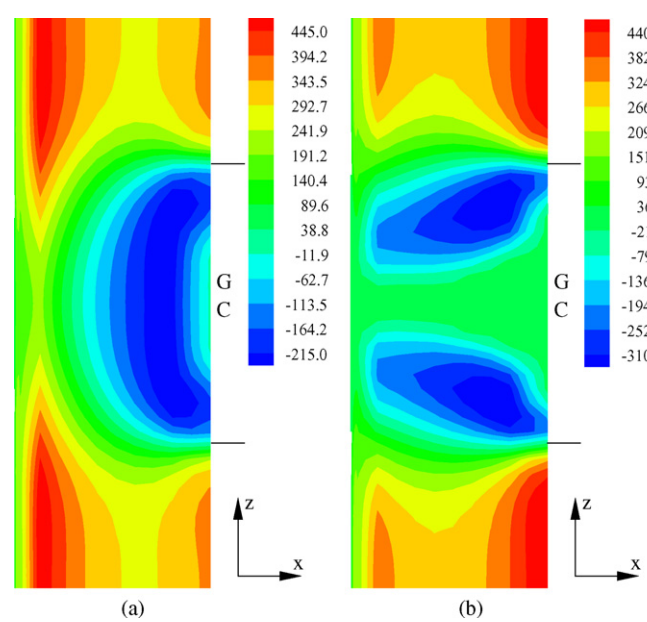

Fig. 10. Distribution of the volumetric condensation/evaporation rate under two different thermal conductivities of the porous materials: (a) 3 W(m K)$^{-1}$, and (b) 1.5 W(m K)$^{-1}$ (unit: mol(m^3 s)$^{-1}$).

the diffusion medium. Of course, this effect has not been incorporated in the present two-phase PEM fuel cell model, and this hypothesis still needs further verification and will be considered in the future modeling efforts.

4. Conclusion

In this paper, a two-phase non-isothermal PEM fuel cell model, which is based on the previously developed mixed-domain PEM fuel cell model with a consistent treatment of water transport in MEA, has been established using the traditional two-fluid method to account for the finite-rate condensation/evaporation phenomena and allow slight water vapor over-saturation. This two-phase PEM fuel cell model could fully incorporate both the anode and cathode sides, properly account for the various water phases, including water vapor, water in the membrane phase, and liquid water, and truly enable numerical investigations of water and thermal management issues with the existence of condensation/evaporation interfaces in a PEM fuel cell.

This two-phase model has been applied herein in a two-dimensional configuration to determine the appropriate condensation and evaporation rate coefficients and conduct extensive numerical studies concerning the effects of the inlet humidity condition and temperature variation on liquid water distribution with or without a condensation/evaporation interface. The condensation rate coefficient determined in this paper, $5000\,s^{-1}$, is consistent with the detailed theoretical analyses in Ref. [33], and it renders the calculated water vapor concentration and liquid water saturation in the porous materials approach the thermodynamic equilibrium condition in real-world operations of PEM fuel cells [43].

Results indicate that the liquid droplet coverage model at the gas diffusion layer and gas channel interface exert significant effects on liquid water distribution and cell performance in a PEM fuel cell. Under a low-humidity inlet condition, a condensation/evaporation interface would appear in the porous materials and its location changes with the inlet humidity value. Under a non-isothermal operation condition with an appropriate thermal conductivity of the GDL, a condensation/evaporation interface could also appear, resulting in a dry region in the porous materials directly under the gas channel, a result consistent with the experimental observations.

Numerical simulations show that liquid water is mainly produced in the GDL in two regions; one is near the current-collecting land owing to the low temperature and another further inside the GDL but still away from the catalyst layer. This result suggests a new role of the micro-porous layer that is at least at the inlet region of the cell, it serves to prevent liquid water from entering the catalyst layer and thus prevent severe liquid flooding in the region. This hypothesis needs to be further verified and considered in the future modeling efforts.

Acknowledgements

This work is partially supported by The Ministry of Personnel of P.R. China and The Department of Personnel of Zhejiang Province (J20070016).

References

[1] S. Um, C.Y. Wang, K.S. Chen, J. Electrochem. Soc. 147 (2000) 4485.
[2] S. Dutta, S. Shimpalee, J.W. Van Zee, Int. J. Heat Mass Transfer 44 (2001) 2029.
[3] N.P. Siegel, M.W. Ellis, D.J. Nelson, M.R. von Spakovsky, J. Power Sources 115 (2003) 81.
[4] S. Mazumder, J.V. Cole, J. Electrochem. Soc. 150 (2003) A1503.
[5] H. Meng, C.Y. Wang, J. Electrochem. Soc. 151 (2004) A358.
[6] H. Meng, C.Y. Wang, Chem. Eng. Sci. 59 (2004) 3331.
[7] B. Hum, X.G. Li, J. Appl. Electrochem. 34 (2004) 205.
[8] G. Hu, J. Fan, S. Chen, Y. Liu, K. Cen, J. Power Sources 136 (2004) 1.
[9] W.Q. Tao, C.H. Min, X.L. Liu, Y.L. He, B.H. Yin, W. Jiang, J. Power Sources 160 (2006) 359.
[10] V. Gurau, H. Liu, S. Kakac, AICHE J. 44 (1998) 2410.
[11] T. Berning, D.M. Lu, N. Djilali, J. Power Sources 106 (2002) 284.
[12] M. Hu, A. Gu, M. Wang, X. Zhu, L. Yu, Energy Convers. Manage. 45 (2004) (1861).
[13] B.R. Sivertsen, N. Djilali, J. Power Sources 141 (2005) 65.
[14] H. Meng, J. Power Sources 162 (2006) 426.
[15] H. Meng, J. Power Sources 164 (2007) 688.
[16] Z.H. Wang, C.Y. Wang, K.S. Chen, J. Power Sources 94 (2001) 40.
[17] L. You, H. Liu, Int. J. Heat Mass Transfer 45 (2002) 2277.
[18] S. Mazumder, J.V. Cole, J. Electrochem. Soc. 150 (2003) A1510.
[19] U. Pasaogullari, C.Y. Wang, J. Electrochem. Soc. 152 (2005) A380.
[20] Y. Wang, C.Y. Wang, J. Electrochem. Soc. 153 (2006) A1193.
[21] T. Berning, N. Djilali, J. Electrochem. Soc. 150 (2003) A1598.
[22] W. He, J.S. Yi, T.V. Nguyen, AICHE J. 46 (2000) 2053.
[23] D. Natarajan, T.V. Nguyen, J. Electrochem. Soc. 148 (2001) A1324.
[24] G. Lin, T.V. Nguyen, J. Electrochem. Soc. 153 (2006) A372.
[25] H. Meng, C.Y. Wang, J. Electrochem. Soc. 152 (2005) A1733.
[26] K. Tüber, D. Pócza, C. Hebling, J. Power Sources 124 (2003) 403.
[27] X.G. Yang, F.Y. Zhang, A.L. Lubawy, C.Y. Wang, Electrochem. Solid-State Lett. 7 (11) (2004) A408.
[28] H. Ju, G. Luo, C.Y. Wang, J. Electrochem. Soc. 154 (2007) B218.
[29] G. Luo, H. Ju, C.Y. Wang, J. Electrochem. Soc. 154 (2007) B316.
[30] H. Ju, Ph.D. Thesis, The Pennsylvania State University (2006).
[31] S. Um, C.Y. Wang, J. Power Sources 156 (2006) 211.
[32] A.A. Kulikovsky, J. Electrochem. Soc. 150 (2003) A1432.
[33] J.H. Nam, M. Kaviany, Int. J. Heat Mass Transfer 46 (2003) 4595.
[34] A.A. Shah, G.S. Kim, W. Gervais, A. Young, K. Promislow, J. Li, S. Ye, J. Power Sources 160 (2006) 1251.
[35] G. Lin, W. He, T.V. Nguyen, J. Electrochem. Soc. 151 (2004) A1999.
[36] C.Y. Wang, P. Cheng, Adv. Heat Transfer 30 (1997) 93.
[37] U. Pasaogullari, C.Y. Wang, J. Electrochem. Soc. 151 (2004) A399.
[38] H. Ju, H. Meng, C.Y. Wang, Int. J. Heat Mass Transfer 48 (2005) 1303.
[39] Y. Wang, C.Y. Wang, J. Electrochem. Soc. 152 (2005) A445.
[40] M. Khandelwal, M.M. Mench, J. Power Sources 161 (2006) 1106.
[41] A. Turhan, K. Heller, J.S. Brenizer, M.M. Mench, J. Power Sources 160 (2006) 1195.
[42] U. Pasaogullari, C.Y. Wang, Electrochim. Acta 49 (2004) 4359.
[43] C.Y. Wang, Chem. Rev. 104 (2004) 4727.